RSC Advances

ROYAL SOCIETY OF CHEMISTRY

www.rsc.org/advances

Cite this: DOI: 10.1039/c0xx00000x

www.rsc.org/xxxxxx

ARTICLE TYPE

Self-assembled hollow urchin-like $NiCo_2O_4$ microspheres for aqueous asymmetric supercapacitors

Ying Lei[a], Yanyan Wang[a], Wen Yang[a], Hongyan Yuan[a] and Dan Xiao [a,b,*]

Received (in XXX, XXX) Xth XXXXXXXXX 20XX, Accepted Xth XXXXXXXXX 20XX
DOI: 10.1039/b000000x

Self-assembled hollow urchin-like microsphere has been synthesized by low temperature coprecipitation approach by employing weakly alkaline $NaHCO_3$ as a generator of gas bubbles and precipitant and CTAB as a structure modifier. The as-prepared hollow precursor can be easily calcined into crystalline $NiCo_2O_4$. The crystal structures, morphologies, sizes and porous properties, and the formation mechanism of the hollow urchin-like microspheres (HUMs) have been investigated carefully as well as the role of the CTAB. Compared with the $NiCo_2O_4$ HUMs without the assistance of CTAB, the CTAB-assisted $NiCo_2O_4$ HUMs (denoted as NC-C) applieded in supercapacitor exhibit enhanced capacitance properties and application potential. An asymmetric supercapacitor (ASC) has been successfully constructed from the NC-C as positive electrode and activated carbon (AC) as negative electrode. The fabricated NC-C//AC ASC with an extended stable operational voltage of 1.6 V can deliver a relative high specific capacitance of 95 F g^{-1} at a current density of 1 A g^{-1} and still maintain 63 F g^{-1} at 20 A g^{-1}. What's more, the NC-C//AC ASC demonstrates remarkable energy density (~36 Wh kg^{-1} at 852 W kg^{-1}), high power density (~11.9 kW kg^{-1} at 16.5 Wh kg^{-1}) and moderate cycleability towards long time charge-discharge test.

1. Introduction

The growing societal and environmental requirements have stimulated the development of sustainable and efficient energy storage systems. Electrochemical capacitors (ECs), also called supercapacitors, are considered one of the most promising candidates for energy storage due to their higher power density, longer cycle-life and much safer than that of batteries, and greater energy storage capacity than that of conventional capacitors.[1-3] However, to meet the increasing energy demands, the energy density of supercapacitors should be raised without sacrificing the power density and cycle life.[2, 4, 5] Energy density (E) can be calculated from the simplified equation[6,7] $E = \frac{1}{2} C \Delta V^2$, and thus energy density of supercapacitors can be efficiently improved by increasing the specific capacitance (C) and/or the cell voltage (ΔV). Researches show that the voltage window increased to 3.0 V by employing organic electrolytes. However, their large-scale commercial applications are restricted by the poor ionic conductivity, toxic nature and high cost. Fortunately, the development of asymmetric supercapacitors (ASCs) consisting of a battery-type Faradaic electrode with high energy and a capacitor-type electrode with desirable power opens a new avenue for boosting the voltage window and energy density. What's more, aqueous ASCs can employ more environmentally friendly aqueous electrolyte endowed with higher ionic conductivity as electrolyte. Many reports aiming at enhancing the energy density by exploring various materials in ASCs, such as graphene-supported $Ni(OH)_2$-nanowires//CMK-5,[8] MnO_2// carbon,[5] VOx//VN,[9] $NiCo_2O_4$@MnO_2//AC ASC device[4] have emerged.

Spinel nickel cobaltite ($NiCo_2O_4$) exhibits intriguing energy storage performance due to its abundance and environmental friendliness, and more importantly, the possible synergetic enhancement such as better electrical conductivity and electrochemical activity due to its richer redox reaction from both nickel and cobalt ions than that from single component oxide.[10] Various $NiCo_2O_4$ materials with diverse structures such as nanowires,[11] nanosheets,[1] and flower-like structure [12] exhibit distinct difference in their capcitance performance. Hollow structures with controllable size and shape endowed with highly specific morphology and novel properties have sparked intense interest among chemists and materials scientists. Furthermore, hollow structures are considered to hold more handles to deliver enhanced performance in different application fields such as catalysis,[13, 14] chemical sensors,[15] drug delivery[16] and energy storage[17]. Specifically, towards energy-related systems, the hollow structures may achieve better specific capacity and rate capability due to their high density of defects arising from nanometer-sized sub-building blocks, large specific surface area (SSA) and long transport lengths for both mass and charge transport.

In the wake of rapid advancements in synthetic strategies, various methods such as template methods,[18] Ostwald ripening-related hydrothermal method,[19] oriented self-assembly,[20] and chemically induced self-transformation[21] have been developed to obtain hollow spheres. Among them, soft template method is an effective one for synthesizing hollow micro-/nanostructures. Gas bubbles can create stable emulsions and foams when dispersed in

a liquid host, which makes them promising soft templates for synthesis of hollow structures. [22] With the aid of gas bubble templates, some hollow structures, such as $CaCO_3$,[23] VOOH[24] and TiO_2 hollow spheres,[25] have been successfully synthesized. Based on the bubbles-induced hollow structure mechanism, hollow structures can be easily obtained just by continuously providing gas to the reaction system without adding any additive as template.

Herein, we designed a low temperature coprecipitation approach to synthesize hollow urchin-like superstructured precursors by skillfully employing weakly alkaline $NaHCO_3$ as a generator of gas bubbles and precipitant and cetyltrimethyl ammonium bromide (CTAB) as structure modifier. The hollow precursors are easily calcined to porous $NiCo_2O_4$ with well-conserved hollow structures. The CTAB-assisted hollow urchin-like $NiCo_2O_4$ (NC-C) microspheres acting as electrode materials for supercapacitors deliver improved electrochemical stability. To demonstrate the principle of boosting energy density, asymmetric suprcapacitors (ASCs) are constructed by employing the NC-C for the positive electrode and activated carbon (AC) for the negative electrode, and the ASCs device (NC-C//AC ASC) have extended the cell voltage to 1.6 V in 6 M KOH aqueous electrolyte, achieving remarkable energy density (~36 Wh kg^{-1}), high power density and moderate cycling stability.

2. Experimental

2.1 Materials Synthesis

All the analytical grade chemicals are commercially available and were used as received. Triply distilled water was used during all the experimental processes. In a typical experiment, 0.65 g $Co(CH_3CO_2)_2$ $4H_2O$, 0.32 g $Ni(CH_3CO_2)_2$ $4H_2O$ and 0.36 g CTAB were dissolved in 50 mL triply distilled water to obtain aqueous solution A, and aqueous solution B was obtained by dissolving 1.26 g $NaHCO_3$ in 50 mL triply distilled water. After stirring for 20 min, aqueous solution B was dropwise added into the aqueous solution A with gentle stir by employing constant pressure drop funnel and the reaction was kept at 35 ^oC all over the process. The clear solution gradually became opaque following the process proceeding. After about 6 h, the aqueous solution B was added over and then the reaction mixture was kept as it was for 6 h. The pink purple precipitates were collected by centrifugation and washed with triply distilled water and ethanol for several times. The precursors were dried in a vacuum at 60 ^oC overnight and then annealed at 250 ℃ under air for 2 h. For the control group without addition of CATB, the same mole ratio of the other reactants and similar procedures was employed. The final products were denoted as NC-C (with addition of CTAB) and NC-0 (the control group without addition of CTAB), respectively.

2.2 Characterization

Crystallite structure of the hollow microsphere samples was established on a Tongda TD-3500 X-ray powder diffractometer (Liaoning, China) with Cu-Kα radiation (λ=0.15148 nm) operating at 30.0 kV and 20.0 mA. The X-ray photoelectron spectra (XPS) were obtained from a Kratos XSAM 800 spectrometer (Manchester, U.K.) with a Mg-Ka X-ray (1253.6 eV) excitation source running at 15 kV, a hemi-spherical electron energy analyzer and a multichannel detector. Fielde-mission scanning electron microscopy (FESEM) images were acquired on a Hitachi S4800 scanning electron microscope (Tokyo, Japan) to examine the morphology of the products. Morphologies of the detail structures were measured with a FEI Tecnai G2 20 high-resolution transmission electron microscope (TEM) (Hillsboro, OR, USA). N_2 adsorption/desorption was determined by Brunauer-Emmett-Teller (BET) measurements using a QuadrasorbTM SI Automated Surface Area and Pore Size Analyzer (Quantachrome, Instruments, Boynton Beach, FL, USA).

2.3 Electrochemical Measurement

The working electrode was prepared with the active material, acetylene black and polyvinylidene fluoride (PVDF) binder in a weight ratio of 80:15:5. A small amount of N-methylpyrrolidinone was then added to the mixtures and then the slurries were cautiously coated on the nickel foam substrates (surface, 1 cm × 1 cm). After dried at 80 ^oC for 2 h, the as-formed electrodes were then pressed at 10 MPa and then further dried at 80 ^oC for 12h before use. The mass loading of active materials in a nickel foam electrode was about 2.5~3.5 mg cm^{-2}. The obtained active material modified electrode was then used as a working electrode.

A typical three-electrode glass cell equipped with a working electrode, a graphite sheet counter electrode, and an Hg/HgO reference electrode was employed for electrochemical measurements of the as-prepared working electrodes. All the electrochemical measurements of the as-obtained samples were carried out on an Autolab PGSTAT 30/302 electrochemical workstation (Eco Chemie B.V., Amsterdam, the Netherlands). The electrochemical properties of the as-synthesized $NiCo_2O_4$ modified electrode were evaluated by cyclic voltammetry (CV), galvanostatic charge-discharge (GCD) and electrochemical impedance spectroscopy (EIS) in 6.0 M KOH solution at ambient conditions. EIS measurements were conducted by applying an AC voltage with 10 mV amplitude in a frequency range from 100 kHz to 0.01 Hz at open circuit potential.

The aqueous asymmetric supercapacitor was fabricated by a piece of NC-C electrode (positive) and AC electrode (negative) with a non-woven fabric separator sandwiched in between. The as-formed electrodes were then pressed at 10 MPa and then soaked in 6 M KOH solution for about 24 h. After that, the aqueous sandwiched asymmetric supercapacitor was tightly encapsulated by parafilm and plastic tape to avoid leakage of the electrolyte. For the NC-C//AC ASCs, the CV and GCD and EIS tests were performed in a two-electrode cell at the 6.0 M KOH aqueous electrolyte.

The GCD test was used to evaluate the capacitance performance of the as-synthesized NC-C, NC-0 and the ASCs. The specific capacitance (SC) was calculated from the following equation [26]:

$$C = \frac{I\ \Delta t}{m \Delta V} \qquad (1)$$

where C, I, Δt and ΔV are the SC (F g^{-1}) of the electrodes, the discharge current (A), the discharge time (s) and the discharge potential range (V), respectively.

3. Results and discussion

3.1 Physicochemical Characterization

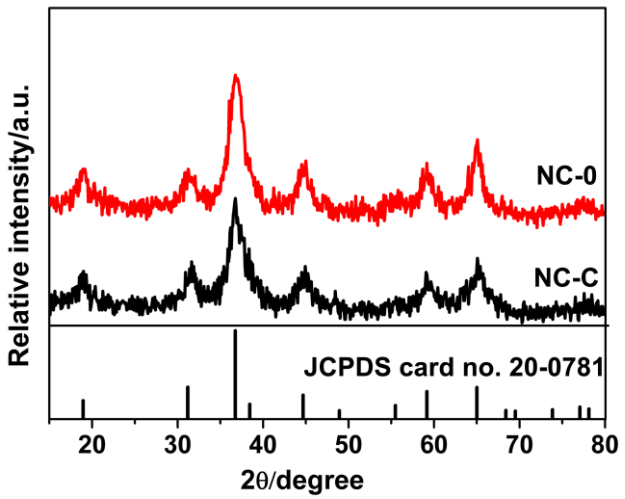

Fig. 1 XRD patterns of the as-synthesized NC-C (black) and NC-0 (red), and the black straight line represents the standard pattern of JCPDS card no. 20-0781

After calcination at 250 °C for 2 h, the pink purple precursors turned to black $NiCo_2O_4$ powder. The Fig. 1 displays the corresponding XRD patterns of the as-synthesized NC-C (black line) and NC-0 (red line), and distinguishable diffraction peaks can be observed. There is no obvious difference in the diffraction peak positions. However, the relative intensity of some diffraction peaks are slightly different, suggesting that the surfactant CTAB have an effect on the crystallinity of products. All of the diffraction peaks at 2 θ =18.9°, 31.2°, 36.7°, 44.6°, 55.4°, 59.1°, 64.9 ° and 77 ° can be respectively assigned to (111), (220), (311), (400), (422), (511), (440) and (533) planes of the spinel $NiCo_2O_4$ (JCPDS card No. 20-0781), and almost no any impurity peak presents in the XRD pattern. Clearly, the results demonstrate that the precursor can be fully converted to $NiCo_2O_4$ at 250 °C for 2 h.

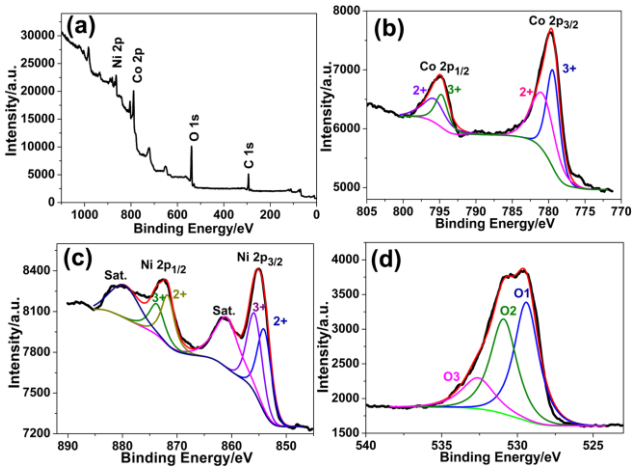

Fig. 2 XPS spectra of (a) survey spectrum, (b) Ni 2p, (c) Co 2p and (d) O 1s for the as-synthesized NC-C.

XPS measurements are implemented to discern the more detailed elemental makeup and the oxidation state of as-prepared NC-C. The survey spectrum (Fig. 2a) shows that only the Co, Ni and O element can be detected obviously. By using a Gaussian fitting method, the Co 2p emission spectrum (Fig. 2b) is best fitted with two spin-orbit doublets characteristic of $Co^{2+}$and Co^{3+}.[27, 28] In Ni 2p spectra (Fig. 2c), two kinds of Ni species can also be observed and assigned to the species containing Ni(II) and Ni(III) ions.[29] In addition, two shakeup satellites (identified as "Sat.") are also obvious. The high-resolution spectrum for O 1s (Fig. 2d) suggests three oxygen species marked as O1, O2 and O3. The fitting peak of O1 at 529.5 eV is typical of metal-oxygen bond. [28, 30] As respect to the component O2, the fitting peak sitting at 531eV is commonly associated with defects, contaminants, and a number of surface species including hydroxyls, chemisorbed oxygen, under-coordinated lattice oxygen, or species intrinsic to the surface of the spinel. [27, 28]The peaks at ~532.7 eV could be attributed to multiplicity of physi- and chemisorbed water on and within the surface.[28, 30] The peaks of O 1s spectrum at binding energies of 529.5 and 531 eV are ascribed to O^{2-} species in $NiCo_2O_4$. These fitting results show that the chemical composition of the NC-C contain Co^{2+}, Co^{3+}, Ni^{2+} and Ni^{3+}, which are consistent with the results in the previous reports for $NiCo_2O_4$. [1, 28]

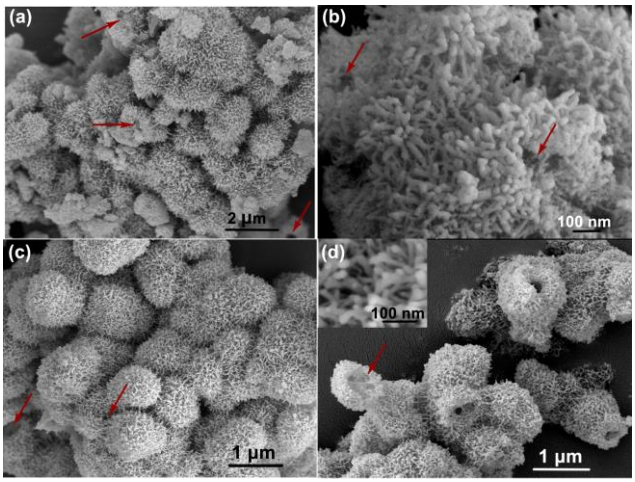

Fig. 3 SEM images of (a, b) the as-obtained NC-0 precursors and (c, d) the as-prepared NC-C precursors. (Arrows point to the hollow cavities)

The morphological and structural features of the as-synthesized hollow precursors are examined by SEM. Fig. 3a and c displays the general view of the as-obtained precursors of NC-0 and NC-C with hollow urchin-like microsphere structures. Compared with the precursors of NC-0, that of the NC-C hold more uniform urchin-like morphology with diameter of about 1.5 μm. It is could be explained that surfactant CTAB can effectively reduce the surface energy of nanoparticles and decrease aggregation, but also can facilitate anisotropic growth of nanocrystals.[31] To further discern the hollow structures, some cracked microspheres are shown in Fig. 3b and d. It is obvious that these microspheres are with hollow cavities, and the hollow cavities are surrounded by the building blocks of nanowires with diameter of about 10~20 nm (Fig. 3b and inset of Fig. 3d).

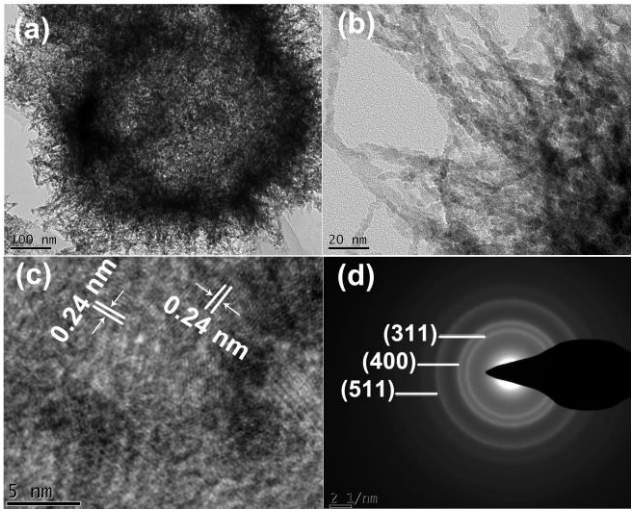

Fig. 4 (a, b) TEM images, (c) HRTEM image and (d) SAED pattern of the as-synthesized NC-C.

We further fell back on TEM, HRTEM and selected-area electron diffraction (SAED) to identify the detailed morphological and crystallographic properties of the as-fabricated NC-C. Typical TEM image in Fig. 4a displays a whole urchin-like microsphere composed of wire-like nanostructures built by the building blocks of nanoparticles. Notably, the result illustrates that the as-prepared NC-C still maintains the intact microsphere morphology, which is consistent with the results from the SEM image of Fig. 3c and d. The magnified TEM image (Fig. 4b) shows that nanowires with transparent feature on their edges are decorated with porous structures on their surfaces, which infers that it could be endowed with high SSA. The hollow cavity is located in the core of the microsphere and the thickness of the walls around the hollow cavity is about 100 nm, which may be beneficial to form ion-buffering reservoirs at the center and shorten ion-transport pathway.[7] The HRTEM image (Fig. 4c) of an individual nanopetal with randomly orientated lattice phase reveals the polycrystalline characteristic of the as-harvested product. In addition, in the HRTEM image, the clearly resolved lattice fringes can be discerned and the lattice spacing is calculated to be about 0.24 nm corresponding to the (311) plane of spinel $NiCo_2O_4$. This result is in accord with that from the previous reports[10, 32]. The SAED pattern (Fig. 4d) displays well-defined rings, which further confirms that the samples are of polycrystalline nature, which is identical with the aforementioned results from XRD and HRTEM.

To better understand the reaction mechanisms responsible for the formation of the hollow urchin-like microspheres, we carried out time-dependent experiment. On the basis of the precusor morphology as a function of reaction time (Fig. S1) and the SEM results from Fig. 3, a probable formation process is proposed in Scheme 1.

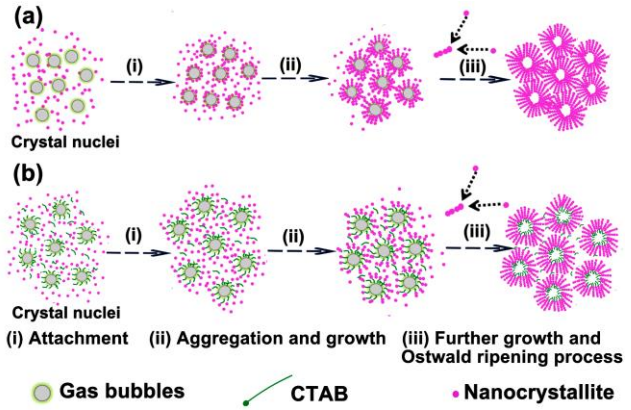

Scheme 1. Schematic illustration of the morphological evolution of hollow urchin-like microspheres (a) without CTAB and (b) with CTAB

Here, metal cations (Co^{2+} and Ni^{2+}) react with CO_3^{2-} and OH^- anions slowly released from hydrolysis of $NaHCO_3$ in an aqueous solutionin, which leads to the formation of precursors. As shown in Fig. S2, the precursor is a mixture of cobalt/nickel hydroxide carbonate salts $Co(CO_3)_{0.5}(OH).nH_2O$ (JCPDS card no. 48-0083) and $Ni_2CO_3(OH)_2$ (JCPDS card no. 35-0501). The relevant reactions can be expressed as follows:

$$HCO_3^- \rightarrow H^+ + CO_3^{2-}$$

$$HCO_3^- + H_2O \rightarrow OH^- + H_2CO_3$$

$$H_2CO_3 \rightarrow H_2O + CO_2$$

$$(Co^{2+}, Ni^{2+}) + xOH^- + 0.5(2-x)CO_3^{2-} + nH_2O$$
$$\rightarrow (Co,Ni)(OH)_x(CO_3)_{0.5(2-x)}.nH_20$$

In the case, CO_2 gas released from hydrolysis of $NaHCO_3$ can create stable emulsions and foams in aqueous solution leading to formation of gas bubble templates.[22] A large number of CTAB surfactant molecules selectively adsorb on the surfaces of gas bubble templates. In the initial reaction stage, a large portion of initial crystal nucleus start to come into being. As the freshly formed nanonuclei are thermodynamically unstable due to their high surface energy, they tend to gather around the interface of CO_2 gas and water (Scheme 1. a) or of CTAB and water (Scheme 1. b) to minimize the interfacial energy, and thus the supersaturated nuclei aggregate together.[33-35] These aggregates then serve as nucleation centres that allow the subsequent adsorption of newly formed nuclei and the growth of primary crystals. Affected by the different electronic structure of Co^{2+} (prefer octahedral coordination) and Ni^{2+} (prefer square-planar coordination), the growth along the c-axis is the fastest leading to the formation of nanowires.[31] Crystal growth and aggregation at the interfaces of gas/liquid and CTAB/liquid leads to transcriptive imprinting of the inner template morphology and formation of initial hollow structures. The initial hollow cavities inside the superstructures are unstable once the gas bubbles burst. Subsquently, the primary hllow structures may suffer from a Ostwald ripening process [19] and as reaction time prolongs, they gradually blossom into robust and well-rounded hollow urchin-like superstructures. It is worth noting that the surfactant CTAB molecules play three roles in generating the hollow structure, i.e., selective adsorption, occupied effect, and prevention of agglomeration of urchin-like superstructures.

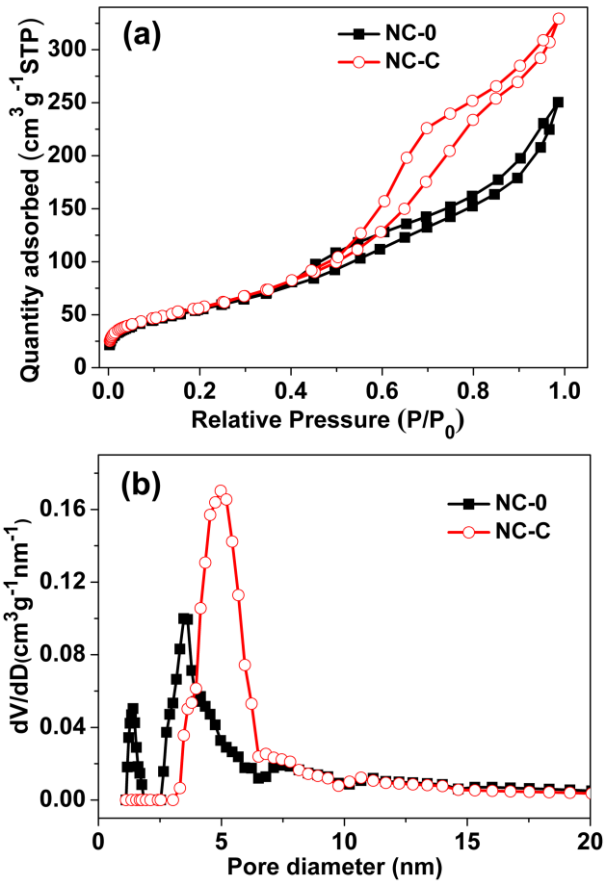

Fig. 5 (a) Nitrogen adsorption-desorption isotherm of NC-C and NC-0 HUMs and (b) their corresponding pore size distribution.

We fell back on Nitrogen (77.3 K) adsorption and desorption experiments to inspect the surface area characterization of the $NiCo_2O_4$ microspheres. Fig. 5a shows the adsorption-desorption isotherm of the NC-C and NC-0 with an obvious hysteresis loop in the range of ca.0.5–1.0 P/P_0, which indicates the existence of a large number of mesoporous structures.[36, 37] According to Brunauer-Emmett-Teller (BET) analysis, the NC-C and the NC-0 hold relatively high SSA of 214 and 200 $m^2\ g^{-1}$, respectively. Both of their SSA are much higher than previous reports[10, 12, 32], which could benefit from their rich porous structure and inside hollow cavities caused by CO_2 gas bubbles. The higher SSA of the NC-C than that of the NC-0 may be attributed to the occupied effect of the CTAB placeholder moleculars, because the remoal of CTAB moleculars can lead to more porous structure. The corresponding pore size distribution (Fig. 5b) calculated by the Barrett-Joyner-Halenda (BJH) method from the desorption branch further confirms the characteristic of mesoporous structure. The pore size distribution of the NC-C mainly centres in the range of 3~10 nm considered to be the optimal pore size for the diffusion of ions and electrons within electrodes.[11] while the pore size distribution of the NC-0 is located in 1.5 nm and 4 nm indicating the existance of mesoporous and a small part of micropores (<2nm). The relatively high SSA and appreciate porous structures of the NC-C could facilitate transport and migration of the electrolyte ions to the internal active sites during charge-discharge process, and thus the NC-C are expected to deliver enhanced capacitance performance.

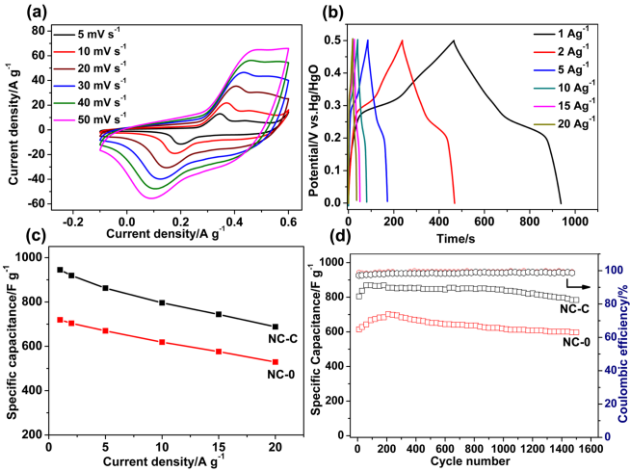

Fig. 6 Electrochemical properties of hollow $NiCo_2O_4$ microspheres: (a) CV curves at different scan rates, (b) GCD curves at different current densities, (c) the corresponding specific capacitance as a function of current density and (d) cycle performance at a current density of 6 A g^{-1} (NC-C (black), NC-0 (red)).

The electrochemical capacitive performance of the as-synthesized $NiCo_2O_4$ is initially carried out in a three-electrode configuration. Fig. 6a and Fig. S3a respectively depict representative CV curves of the NC-C and NC-0 measured at various scan rates ranged from 5 to 50 mV s^{-1} in a potential range of -0.1~0.6 V (*vs.* Hg/HgO) in 6.0 M KOH solution. Two well-defined redox peaks can be observed in anodic and cathodic sweeps in all CV curves. The redox peaks are mainly attributed to the following redox reactions:[38]

$$NiCo_2O_4 + OH^- + H_2O \leftrightarrow NiOOH + 2CoOOH + 2e^-$$

$$CoOOH + OH^- \leftrightarrow CoO_2 + H_2O + e^-$$

However, interestingly, there are no two couples of redox peaks corresponding to redox couples of Ni^{2+}/Ni^{3+} and Co^{2+}/Co^{3+}, which could be ascribed to the similar redox potential of Co_3O_4 and NiO and the surface modification of $NiCo_2O_4$ by conductive acetylene black which can induce appreciable broadening of some redox peaks. [39] For both NC-C and NC-0, all CV curves (Fig. 6a, Fig. S3a) exhibit the similar shape and the peak current increase with increasing scan rates. The shape of CVs changes little even at the high scan rate of 50 mV s^{-1}, indicating their good kinetic reversibility of the $NiCo_2O_4$ modified electrodes.

Galvanostatic charge-discharge (GCD) measurements are implemented to quantify the SCs and rate capability of the hollow $NiCo_2O_4$ active materials. Obviously, the nonlinearity in the GCD curves (Fig. 6b and Fig. S3b) further verifies the pseudocapacitance behavior of $NiCo_2O_4$. Fig. 6c shows the capacitance value of NC-C and NC-0 at different current densities. Obviously, the specific capacitance of NC-C electrode is much higher than those of the NC-0 electrode at the same current density. Understandably, benefiting from the richer porous nanostructures of the NC-C, numerous electroactive sites can be better utilized to boost the capacitive performance considerably. In addition, with the increase of current density, the corresponding specific capacitance trends to decrease. The capacitance value of both NC-C and NC-0 at 20 A g^{-1} remain to be around 73% of that obtained at the current density of 1 A g^{-1} revealing their good rate capabilities. Compared to the other reported $NiCo_2O_4$ electrode materials[1, 10, 11], the SC value of the $NiCo_2O_4$ HUMs is moderate, but the capacitance retention is outing. For both of the $NiCo_2O_4$ HUMs, the inside hollow cavities acting as an "ion-buffering reservoir" facilitate quicker permeation process of electrolyte into each electroactive unit by

shortening the diffusion distance of OH^-, and accommodate the arisen strain caused by high rate insertion and extraction of OH^- ions.[39]

In order to investigate the service life and stability, the charge-discharge cyclic performance at a current density of 6 A g^{-1} is tested. Fig. 6d shows the SCs of the NC-C and NC-0 electrodes against the cycle number. Obviously, capacitance retention ration of the NC-C (about 93.6% of the maximum SC) is much higher than that of the NC-0 (85%) after 1500 continuous charge-discharge cycles. Their coulombic efficiency remains above 97% over the extended charge-discharge cycles. These results demonstrate the NC-C holds higher SC and more excellent cycling stability than that of the NC-0. The enhanced capacitance performance of the NC-C enables it to be a promising candidate for high-performance pseudocapacitors.

To further evaluate the practical application of NC-C electrode in a full-cell setup, an asymmetric supercapacitor was constructed by using the NC-C electrode as the positive and the laboratory-prepared AC as the negative electrode (denoted as NC-C//AC). The AC delivers a specific capacitance of 251, 217, 205 and 188 F g^{-1} at a current density of 1, 5, 10 and 20 A g^{-1}, respectively. According to the testing results of $NiCo_2O_4$ and AC electrodes (for details, see Fig. S4†), based on charge balancing principle, the mass ratio of nickel cobalt oxide (m_+) and activated carbon (m_-) can be optimized according to the following equation.[40, 41]

$$\frac{m_+}{m_-} = \frac{C_- \times \Delta E_-}{C_+ \times \Delta E_+} \qquad (2)$$

where m is the mass (g) of electrode, C is the specific capacitance (F g^{-1}) and ΔE is the potential range (V) for the charge-discharge process.

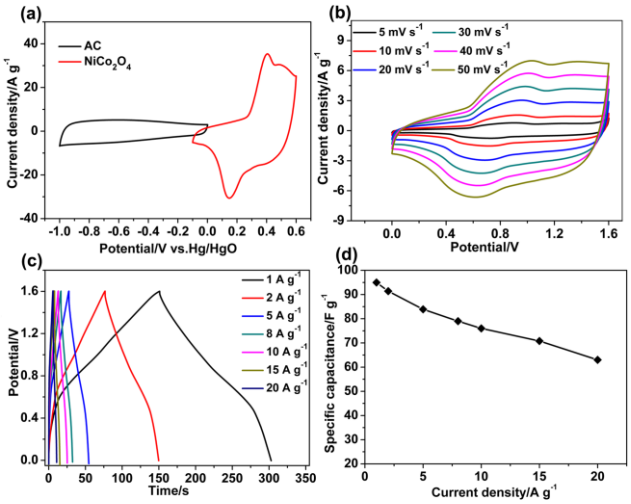

Fig. 7 (a) CV curves of $NiCo_2O_4$ electrode and AC electrode obtained in 6.0 M KOH aqueous solution with a scan rate of 20 mV s^{-1}. (b) CV curves at different scan rates, (c) GCD curves at different current densities, and (d) the corresponding specific capacitance as a function of current density of $NiCo_2O_4$//AC ASCs.

Fig. 7a demonstrates the CV curves of AC-based electrode and as-prepared NC-C electrode at a scan rate of 20 mV s^{-1}. The result indicates that such ASCs can deliver 1.6 V operation voltage which is higher than that of conventional AC-based symmetric supercapacitors (0.8~1.0V). Accordingly, in the subsequent electrochemical performance assessment of the NC-C//AC ASCs, the potential window of 0~1.6 V is employed. Both CV and GCD measurements are carried out to survey the capacitance performance of the NC-C//AC ASCs in a voltage window of 0~1.6 V. Fig. 7b shows CV caves at various scan rates. Fig. 7c displays the GCD caves of the ASCs at different current densities and its corresponding specific capacitance is shown in Fig. 7d. The NC-C//AC ASCs can achieve a specific capacitance of 95, 83.9, 76 and 63 F g^{-1} at the current density of 1, 5, 10 and 20 A g^{-1}, respectively.

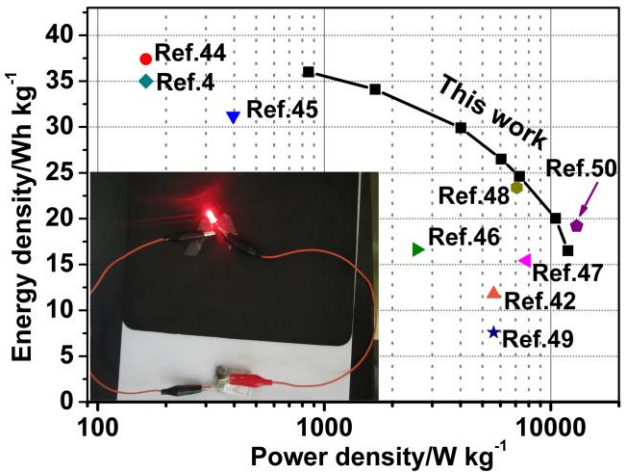

Fig. 8 Ragone plot of the NC-C//AC ASCs. The reported values for others ASCs are provided here for a batter comparison. (Inset shows a red LED powered by the tandem NC-C//AC ASC device)

Power density and energy density are the two key parameters to evaluate the performance of supercapacitors. Based on the GCD curves of the ASC, the energy density (E) and power density (P) could be calculated from the equations: [42]

$$E = (\int I V(t)\, dt)/(m) \qquad (3)$$

$$P = \frac{E}{\Delta t} \qquad (4)$$

where E is energy density (Wh kg^{-1}), P is power density (W kg^{-1}), I is the discharging current, $V(t)$ is discharging voltage excluding the IR drop, dt is time differential, m is the total mass of the positive and negative electrode active materials ($m=m_+ + m_-$) (for details, see the ESI†), and Δt is the discharging time. Fig. 8 depicts the Ragone plot (the energy density as a function of the power density) of the NC-C//AC ASC. With discharge current density increasing from 1 A g^{-1} to 20 A g^{-1}, the energy density decreased from 36 to 16.5 Wh kg^{-1} and the power density increased from 852 W kg^{-1} to 11900 W kg^{-1}, respectively. Obviously, the achieved energy density is higher than that of the symmetrical supercapacitors such as CNTs//CNTs supercapacitors (<10 Wh kg^{-1}).[43] What's more, the specific energy and power density of the NC-C//AC ASCs are compared to the previously reported aqueous asymmetric supercapacitor devices, such as $NixCo_{3-x}O_4$//AC (37.4 Wh kg^{-1} at 163 W kg^{-1}), [44] hierarchical mesoporous $NiCo_2O_4$@MnO_2 core–shell nanowire arrays/AC(35 Wh kg^{-1} at 163 W kg^{-1}),[4] 3D interconnected mesoporous $NiCo_2O_4$@$Co_xNi_{1-x}(OH)_2$ nanosheet arrays //AC(31.2 Wh kg^{-1} at 396 W kg^{-1}),[45] $ZnCo_2O_4$ nanowire cluster arrays//AC(16.63 Wh kg^{-1} at 2561 W kg^{-1}),[46] Hierarchical $NiCo_2O_4$ nanosheets@ hollow microrod arrays//AC (15.42 Wh kg^{-1} at 7800 W kg^{-1}),[47] 3D CoO@ polypyrrole nanowire array electrode//AC(11.8 Wh kg^{-1} at 5600 W kg^{-1}),[42] CoO_x@$Ni(OH)_2$//AC (23.4 W h kg^{-1} at 7080 W kg^{-1}), [48] GNCC//AC (7.6 Wh kg^{-1} at 5600 W kg^{-1})[49] and 3D

Carbon//$CoNi_3O_4$//AC (19.2 Wh kg^{-1} at 13 kW kg^{-1}).[50] Comparison results persuasively display its superior power density and energy density of the NC-C//AC ASC. A simple application to power a commercial light-emitting diode (LED) is demonstrated. After being charged to 3.2 V, the tandem NC-C//AC ASCs with two devices connected in series can light up a red LED (Fig. 8 inset).

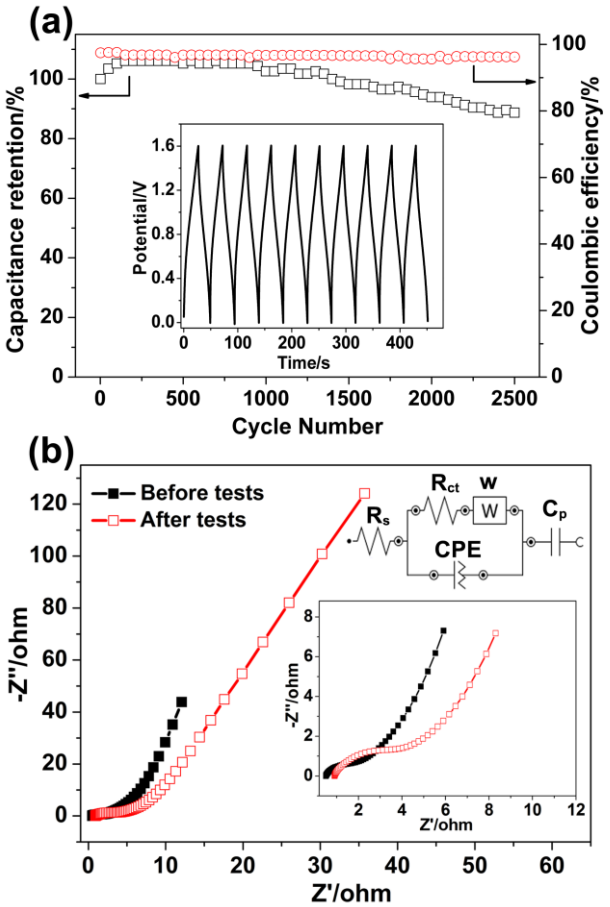

Fig. 9 (a) cycle performance at a current density of 6 A g^{-1} and (b) Nyquist plots of the NC-C//AC ASC before and after cycle test.

A 2500-cycle charge-discharge test at a current density of 6 A g^{-1} is implemented to examine the long-term cycle stability of the as-fabricated ASC. Fig. 9a reveals the outstanding cycling life of our supercapacitor. It displays that the capacity initially has a slight increase due to an "activation process", and the overall specific capacitance can retain at about 88.7% retention after 2500 cycles. Fig. 9a also displays a good electrochemical reversibility with around 97% coulombic efficiency. The inset (Fig. 9a) shows the first 10-cycle GCD curves of the as-fabricated NC-C//AC ASC. The Nyquist plots (Fig. 9b) of the as-fabricated ASC are also employed to investigate the charge-transfer resistance before and after cycling tests. All the impedance spectra, composed of one high frequency semicircle related to R_{ct} followed by one linear component at the low frequency, are almost similar. The Nyquist plots can be well fitted by employing an equivalent circuit (inset of Fig. 9b), where R_s is a bulk solution resistance consisting of the intrinsic resistance of the electroactive materials and the resistance of the KOH electrolyte, and the interface contact resistance, R_{ct} is a Faradaic charge-transfer resistance, CPE is a constant phase element accounting for a double-layer capacitor, and C_p is a pseudocapacitive element.[51] The R_s and R_{ct} can be estimated from the intercept of the high frequency semicircle with the real axis at R_s and (R_s+R_{ct}), respectively. Before and after tests, the bulk solution resistances R_s do not change much. The corresponding charge transfer resistances R_{ct} are 1.04 and 3.20 Ω, respectively. The slightly enlarged charge transfer resistance after cycling tests could be arisen from the destruction of a part of electroactive materials suffering from numerous harsh redox reactions, which is responsible for the specific capacitance drops when the cycling approaches 2500 cycles.

Conclusions

In this work, we have successfully synthesized NC-C HUMs via a facile CO_2 gas bubbles- and CTAB-assisted CATB-assisted low-temperature coprecipitation approach followed by calcining at 250 °C. The hollow urchin-like NC-C superstructures consisting of numerous nanowires exhibit high SSA and porosity. The electrochemical testing results demonstrate that NC-C HUMs as an electrode material for electrochemical capacitors can deliver high specific capacitance of 945 F g^{-1} at 1 A g^{-1}, remarkable rate capability and excellent cycle stability. An asymmetric supercapacitor by the combination of NC-C HUMs as the positive electrode and activated carbon (AC) as the negative electrode can achieve a specific capacitance of 95 F g^{-1} at a current density of 1 A g^{-1} with a stable operational voltage of 1.6 V and a maximum energy density of 36 Wh kg^{-1} at 852 W kg^{-1}. The comprehensive performance evaluation of the hollow urchin-like $NiCo_2O_4$ mesoporous microsphere renders it a promising electrode material for supercapacitor. This reported facile gas bubbles- and CTAB-assisted coprecipitation approach can also be applied for other transition metal oxides and could lead to a positive impact for developing high performance electrochemical energy storage devices.

Acknowledgements

This work was financially supported by the National Natural Science Foundation of China (Nos. 21177090, 21275104 and 21175094).

Notes

[a]*College of Chemical Engineering, Sichuan University, 29 Wangjiang Road, Chengdu 610064, PR China. *Fax: +86-28-85415029. Tel: +86-28-85416029.*
[b]*College of Chemistry, Sichuan University, 29 Wangjiang Road, Chengdu 610064, PR China. *Fax: +86-28-85415029. Tel: +86-28-85416029.*
**Corresponding author: Dan Xiao; E-mail: xiaodan@scu.edu.cn*

† Electronic Supplementary Information (ESI) available: Fig. S1 SEM images of the precusor samples of the NC-0 collected after different reaction time, Fig. S2 XRD pattern of the as-synthesized precursor, Fig. S3 Electrochemical properties of the hollow NC-0 microspheres, Fig. S4 Capacitance properties of the laboratory-prepared activated carbon (AC) and Optimization of mass ratio of $NiCo_2O_4$ and AC. See DOI: 10.1039/b000000x/

References

1. C. Yuan, J. Li, L. Hou, X. Zhang, L. Shen and X. W. D. Lou, *Adv. Funct. Mater.*, 2012, **22**, 4592-4597.
2. J. Jiang, Y. Li, J. Liu, X. Huang, C. Yuan and X. W. D. Lou, *Adv. Mater.*, 2012, **24**, 5166-5180.
3. H. Wang, Q. Gao and L. Jiang, *Small*, 2011, **7**, 2454-2459.
4. K. Xu, W. Li, Q. Liu, B. Li, X. Liu, L. An, Z. Chen, R. Zou and J. Hu, *J. Mater. Chem. A*, 2014, **2**, 4795-4802.
5. V. Khomenko, E. Raymundo-Pinero and F. Béguin, *J. Power Sources* , 2006, **153**, 183-190.
6. W. G. Pell and B. E. Conway, *J. Power Sources* , 2004, **136**, 334-345.
7. D. W. Wang, F. Li, M. Liu, G. Q. Lu and H. M. Cheng, *Angew. Chem. Int. Edit.*, 2008, **47**, 373-376.
8. Y. Wang, D. Zhou, D. Zhao, M. Hou, C. Wang and Y. Xia, *J. Electrochem. Soc.*, 2013, **160**, A98-A104.
9. X. Lu, M. Yu, T. Zhai, G. Wang, S. Xie, T. Liu, C. Liang, Y. Tong and Y. Li, *Nano lett.*, 2013, **13**, 2628-2633.
10. R. Zou, K. Xu, T. Wang, G. He, Q. Liu, X. Liu, Z. Zhang and J. Hu, *J. Mater. Chem. A*, 2013, **1**, 8560-8566.
11. H. Jiang, J. Ma and C. Li, *Chem. Commun.*, 2012, **48**, 4465-4467.
12. L. Li, Y. Cheah, Y. Ko, P. Teh, G. Wee, C. Wong, S. Peng and M. Srinivasan, *J. Mater. Chem. A*, 2013, **1**, 10935-10941.
13. H. M. Chen, R. Liu, M. Lo, S. Chang, L. Tsai, Y. Peng and J. Lee, *J. Phys. Chem. C*, 2008, **112**, 7522-7526.
14. L. Li, Y. Chu, Y. Liu and L. Dong, *J. Phys. Chem. C*, 2007, **111**, 2123-2127.
15. J.-H. Lee, *Sensor. Actuat. B: Chem.*, 2009, **140**, 319-336.
16. J. Yang, J. Lee, J. Kang, K. Lee, J.-S. Suh, H.-G. Yoon, Y.-M. Huh and S. Haam, *Langmuir*, 2008, **24**, 3417-3421.
17. L. Zhou, D. Zhao and X. D. Lou, *Angew. Chem.*, 2012, **124**, 243-245.
18. T. He, D. Chen, X. Jiao, Y. Xu and Y. Gu, *Langmuir*, 2004, **20**, 8404-8408.
19. H. Chun Zeng, *Curr. Nanosci.*, 2007, **3**, 177-181.
20. M. Mo, J. C. Yu, L. Zhang and S. K. Li, *Adv. Mater.*, 2005, **17**, 756-760.
21. J. Yu, H. Yu, H. Guo, M. Li and S. Mann, *Small*, 2008, **4**, 87-91.
22. X. W. D. Lou, L. A. Archer and Z. Yang, *Adv. Mater.*, 2008, **20**, 3987-4019.
23. T. Tomioka, M. Fuji, M. Takahashi, C. Takai and M. Utsuno, *Cryst. Growth Des.*, 2011, **12**, 771-776.
24. C. Wu, Y. Xie, L. Lei, S. Hu and C. OuYang, *Adv. Mater.*, 2006, **18**, 1727-1732.
25. X. Li, Y. Xiong, Z. Li and Y. Xie, *Inorg. Chem.*, 2006, **45**, 3493-3495.
26. M. Liu, L. Kong, C. Lu, X. Li, Y. Luo and L. Kang, *ACS Appl. Mater. Interfaces*, 2012, **4**, 4631-4636.
27. Y. E. Roginskaya, O. Morozova, E. Lubnin, Y. E. Ulitina, G. Lopukhova and S. Trasatti, *Langmuir*, 1997, **13**, 4621-4627.
28. J. Marco, J. Gancedo, M. Gracia, J. Gautier, E. Rıos and F. Berry, *J. Solid State Chem.*, 2000, **153**, 74-81.
29. J. G. Kim, D. Pugmire, D. Battaglia and M. Langell, *Appl. Surf. Sci.*, 2000, **165**, 70-84.
30. T. Choudhury, S. Saied, J. Sullivan and A. Abbot, *J. Phys. D: Appl. Phys.*, 1989, **22**, 1185.
31. X. Shen, J. Sun, G. Wang, J. Park and K. Chen, *Mater. Res. Bull.*, 2010, **45**, 766-771.
32. L. Qian, L. Gu, L. Yang, H. Yuan and D. Xiao, *Nanoscale*, 2013, **5**, 7388-7396.
33. Y. S. Han, G. Hadiko, M. Fuji and M. Takahashi, *Chem. Lett.*, 2005, **34**, 152.
34. Q. Peng, Y. Dong and Y. Li, *Angew. Chem.*, 2003, **115**, 3135-3138.
35. C. L. Jiang, Zhang,W. Q., Zou, G. F.,Yu, W. C., Qian,Y.T., *Nanotechnology*, 2005, **16**, 551-554.
36. K. S. Sing, *Pure.. Appl. Chem.*, 1985, **57**, 603-619.
37. C. Yu, L. Zhang, J. Shi, J. Zhao, J. Gao and D. Yan, *Adv. Funct. Mater.*, 2008, **18**, 1544-1554.
38. X. Wang, X. Han, M. Lim, N. Singh, C. L. Gan, M. Jan and P. S. Lee, *J. Phys. Chem. C*, 2012, **116**, 12448-12454.
39. S. K. Meher and G. R. Rao, *J. Phys. Chem. C*, 2011, **115**, 15646-15654.
40. H. Li, M. Yu, F. Wang, P. Liu, Y. Liang, J. Xiao, C. Wang, Y. Tong and G. Yang, *Nat. commun.*, 2013, **4**, 1894.
41. P. C. Gao, A.-H. Lu and W.-C. Li, *J. Power Sources* , 2011, **196**, 4095-4101.
42. C. Zhou, Y. Zhang, Y. Li and J. Liu, *Nano lett.*, 2013, **13**, 2078-2085.
43. M. Kaempgen, C. K. Chan, J. Ma, Y. Cui and G. Gruner, *Nano lett.*, 2009, **9**, 1872-1876.
44. X. Wang, C. Yan, A. Sumboja and P. S. Lee, *Nano Energy*, 2014, **3**, 119-126.
45. K. Xu, R. Zou, W. Li, Q. Liu, X. Liu, L. An and J. Hu, *J. Mater. Chem. A*, 2014, **2**, 10090-10097.
46. B. Guan, D. Guo, L. Hu, G. Zhang, T. Fu, W. Ren, J. Li and Q. Li, *J. Mater. Chem. A*, 2014, **2**, 16116-16123.
47. X.-F. Lu, D.-J. Wu, R.-Z. Li, Q. Li, S.-H. Ye, Y.-X. Tong and G.-R. Li, *J. Mater. Chem. A*, 2014, **2**, 4706-4713.
48. J. Zhu, L. Huang, Y. Xiao, L. Shen, Q. Chen and W. Shi, *Nanoscale*, 2014, **6**, 6772-6781.
49. H. Wang, C. M. Holt, Z. Li, X. Tan, B. S. Amirkhiz, Z. Xu, B. C. Olsen, T. Stephenson and D. Mitlin, *Nano Res.*, 2012, **5**, 605-617.
50. J. Zhu, J. Jiang, Z. Sun, J. Luo, Z. Fan, X. Huang, H. Zhang and T. Yu, *Small*, 2014, **10**, 1613-6829.
51. K. Liang, X. Tang and W. Hu, *J. Mater. Chem.*, 2012, **22**, 11062-11067.

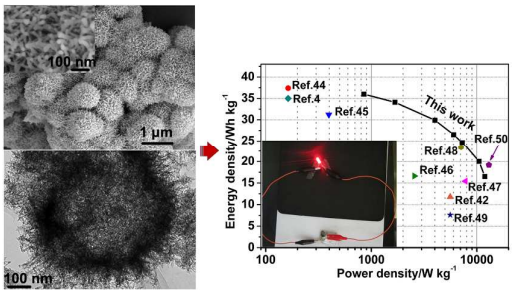

Gas bubbles- and CTAB-assisted low temperature coprecipitation synthesis of hollow $NiCo_2O_4$ microspheres for aqueous asymmetric supercapacitors with remarkable energy density and power density.